

Experimental Loss Segregation in a Solid Rotor Induction Motor

Carlos A. C. Wengerkievich¹ , Nelson J. Batistela¹ , Nelson Sadowski¹ , Thomas Huguet² ,
Yvan Lefèvre² 

¹GRUCAD, Federal University of Santa Catarina (UFSC), Florianópolis, Brazil,
c.a.correa@ufsc.br, jhoebatistela@ufsc.br, nelson.sadowski@ufsc.br

²LAPLACE - Laboratoire Plasma et Conversion d'Énergie, Centre National de la Recherche Scientifique,
University of Toulouse, Toulouse, France, thomas.huguet@toulouse-inp.fr, lefevre@laplace.univ-tlse.fr

Abstract— Solid rotor induction motors (SRIMs) are asynchronous motors suited for high speed applications. This work presents an experimental case study where standard loss segregation procedures for induction motors are performed with a two-phase smooth solid rotor induction motor in order to verify their applicability. Even though the machine is supposed to operate at high frequency, the tests are performed at reduced frequency and voltage in order to avoid the effects of time harmonics. An adjustment in the separation of losses is proposed to contemplate the effects of the high no-load slip, and the behavior of the stray losses under high per-unit slip is analyzed in a load test. The test results are finally extrapolated for the rated condition.

Index Terms— Induction motor, Loss segregation, Solid rotor.

I. INTRODUCTION

Solid rotor induction motors (SRIMs) are asynchronous machines whose rotor is a simple solid steel cylinder that acts both as magnetic and electric circuit, sometimes also featuring longitudinal slits and copper end rings, bars or superficial layers [1], [2]. Some of their advantages over laminated-rotor motors are their higher mechanical strength and thermal ruggedness, simpler manufacture, lower starting current and higher starting torque per ampere [3], [4]. These characteristics make SRIMs well-suited for applications at higher speeds or with severe load cycles [1], [4], [5]. Applications are found in gas compression [2], [3], [6], railway traction [7], medical [8] and generation [5] contexts.

On the other hand, the absence of laminations offers a free path for harmonic currents that increase substantially the rotor losses without producing torque [1]. The increased airgap lengths often employed to mitigate the rotor harmonic losses, combined with the relatively low magnetic permeability of mild steel, tend to result in a lower power factor in comparison to conventional cage motors [9]. Due to this aspect and to the relatively low conductivity of steel, SRIMs also tend to be less efficient [3], even though efficiency levels over 90% can be achieved at higher supply frequencies [2]. Moreover, these motors tend to present less steep torque-speed curves and higher no-load slips [3], [10].

Although SRIMs might at first glance seem equivalent to cage motors with high rotor resistance, its

internal operation features fundamental differences, for instance the virtually constant rotor power factor and the strong dependence of the rotor impedance on the airgap flux [3], that are presented in detail in Section II. These characteristics may hinder the application of traditional test methods for loss segregation in asynchronous motors, such as those featured in the IEEE Standard 112 [11] and in the IEC 60034-2-1 [12] consisting on load and no-load tests.

Few experimental studies have been reported previously on the matter of loss segregation in SRIMs. In [3], efficiency curves were obtained in laboratory tests with a SRIM employed in a gas compressor, where the shaft power was indirectly determined based on the compressor efficiency. A comprehensive study was conducted in [9] where the stray losses of SRIMs were estimated based on the temperature elevation of the rotor. The development of a SRIM for gas compression was reported in [2], and important issues about performance tests were approached, e.g. the use of a 50 Hz power supply instead of the rated 170 Hz, to avoid the effects of time harmonics, and the impracticability of a no-load test in that case, which hindered the experimental determination of the power flow. Different approaches for iron loss calculation were studied in [13], whose results are verified with test results only at no-load condition. The experimental procedure followed in other works [4], [6], [8], [14], [15], was limited to locked-rotor and no-load tests.

In this paper, the applicability of standard methods for loss segregation in induction motors is investigated in the context of SRIMs through a case study with a small two-phase smooth-rotor prototype. The loss segregation procedure featured in method B of the IEEE Standard 112 is adopted as the main reference. Selected theoretical aspects of SRIMs are reviewed in Section II. The standard method for loss segregation is summarized in Section III. The test setup is presented in Section III, and the results are presented and analyzed in Section IV.

II. THEORETICAL ASPECTS OF SRIMs

In cage motors, the rotating magnetic flux in the airgap induces rotor currents that remain mainly confined to the cage bars and end rings made of highly conductive materials such as aluminum or copper. Eddy currents in the laminated rotor core do also exist, but are regarded as a parasite factor that contributes to the stray losses [16]. The rotor flux path is mainly defined by the rotor teeth and yoke geometry with little dependence on the airgap flux intensity, except in extreme conditions.

In a smooth solid rotor, in contrast, the distribution of the magnetic flux and of the induced currents is less predictable. Early electromagnetic models [17], [18] considered the rotor material linear, i.e. with constant permeability, resulting in a flux depth of penetration inversely proportional to the square root of the slip frequency. The equivalent circuit model derived from this approach has a rotor branch with both resistance and reactance inversely proportional to the square root of the slip frequency and numerically equal, thus producing a constant rotor power factor of 0.707.

However, magnetic saturation plays an important role in the behavior of solid rotors. A modelling approach known as limiting nonlinear theory was proposed by McConnell and Sverdup [19] based on

the work of Agarwal [20], where the magnetization curve of a saturated material was simplified as a rectangular function. In this approach, the rotor flux path is considered a saturated superficial layer whose depth is mainly a function of the airgap flux intensity and of the pole pitch, with little influence from the slip frequency. A more intense magnetic flux would require a wider saturated flux path, reaching deeper into the rotor and interacting with more conductive material. The induced currents would thus be distributed over a wider area, facing reduced resistance.

This behavior is illustrated in the induction charts in Fig. 1, obtained via two-dimensional nonlinear time-stepping finite-element-method (FEM) simulations with the geometry of the test machine adopted in this work. The first two charts consider a 50 V, 50 Hz sinusoidal supply. As the slip increases from 0% in the first case to 30% in the second, the depth of penetration in the rotor remains practically the same, as can be seen by the color scale. When the voltage is increased to 70 V, as illustrated in the right chart, the flux reaches noticeably deeper into the rotor.

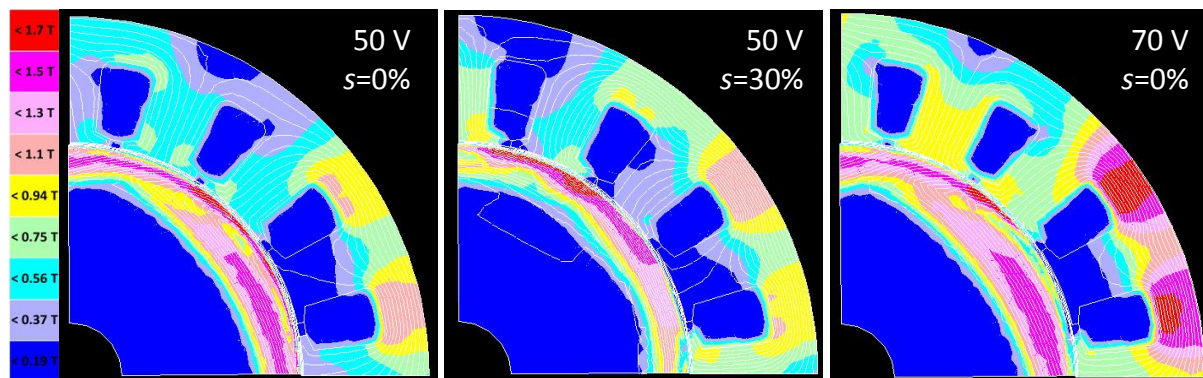


Fig. 1. Induction chart of the SRIM prototype at three different conditions, obtained via 2D time-stepping nonlinear FEM simulations. As the voltage increases, the flux reaches deeper into the rotor.

The equivalent circuit model derived from the limiting nonlinear approach is depicted in Fig. 2, where R_1 and X_1 are the stator winding resistance and leakage reactance, R_c is the core loss resistance, X_m is the magnetizing reactance, Z_r , R_r and X_r are the equivalent rotor impedance, resistance and leakage reactance, all referred to the stator, V_1 is the phase voltage phasor at fundamental frequency f_e , s is the per-unit slip, E is the stator electromotive force (EMF), and I_1 , I_ϕ and I_2 are the phase, excitation and load current phasors, respectively. The parameters R_2 and X_2 , in this case, are respectively the equivalent rotor resistance and reactance normalized by (f_e/sE) , and their dimension is $\Omega \cdot \text{V}/\text{Hz}$. The impedance of the rotor branch proportional to f_e/E translates the dependence on the airgap flux intensity. Both the rotor resistance and reactance vary with slip, and the leakage reactance is numerically equal to half of the resistance, meaning a constant rotor phase angle of 26.6° and power factor of 0.895 [21]. This model has been extensively used for the fundamental frequency effects in SRIMs [4], [7], [22], [23], while the linear approach has been adopted mostly to study the small-signal behavior of harmonic field components [24]-[26].

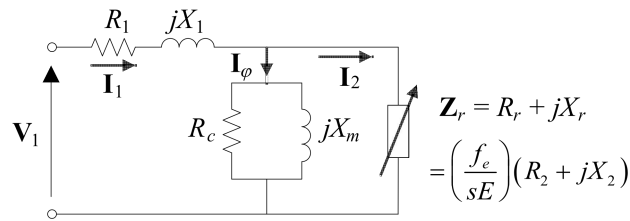


Fig. 2. Equivalent circuit model derived from the limiting nonlinear theory.

The absence of rotor laminations offers a free path for the circulation of high-frequency eddy currents, which arise mainly from the non-sinusoidal distribution of the stator magnetomotive force (MMF), from the non-uniform airgap permeance due to the slot openings and from time harmonics eventually present in the power supply [9]. The losses produced by these currents, usually known as rotor surface losses, can reach levels comparable to the rotor loss at slip frequency [2]. As analyzed by Schwarz [16] and more specifically by Spooner [9], a significant part of these stray losses is present at no-load condition, being hardly dissociable from the core losses [13].

In order to mitigate the surface losses, longer airgaps are commonly adopted in SRIMs [8], [17], among alternatives such as semimagnetic slot wedges, modified notches in the stator teeth [27] and magnetic or conductive layers deposited on the rotor surface [9], [15]. Longer airgaps, combined with the low permeability of mild steel and with the rotor saturation, result in a diminished magnetizing reactance, increased no-load current and lower power factor. On the other hand, the rotor core is sometimes longer than the stator core to accommodate rotor end effects, and the proximity of ferromagnetic material to the end windings results in increased stator leakage reactance [6], [8].

Some insights of special interest for this work can be drawn from this review: i) The electrical characteristics of a SRIM depend strongly on the applied voltage and frequency; ii) Due to the relatively low rotor power factor, the assumption of quadrature between the load and magnetization currents may not be acceptable; iii) The ratio between the stator leakage and the magnetizing reactances can be lower than in conventional motors, thus the stator EMF can differ significantly from the terminal voltage; iv) The stray losses can reach much higher levels in SRIMs. The importance of these aspects on the loss segregation tests will be analyzed ahead.

III. LOSS SEGREGATION IN POLYPHASE INDUCTION MOTORS

Standard tests for loss segregation in polyphase induction motors are described in the IEEE Standard 112 [11] and in the IEC 60034-2-1 [12]. As the featured methods are very similar, the IEEE standard is adopted here as reference for convenience. Its method B, recommended as the preferred option for efficiency determination, consists in resistance measurements, no-load and load tests with input and output power measurements to determine five types of losses: stator joule loss (P_{j1}), core loss (P_c), rotor joule loss (P_{j2}), friction and windage loss (P_{fw}) and stray load loss (P_{sl}).

The procedure starts with the measurement of the DC phase resistance of the stator windings at room temperature. The motor is operated at rated load until it reaches thermal stability, and its rated

temperature elevation is measured with embedded sensors or based on the resistance variation. A load test is performed at six load levels from 150% to 25% of the rated output power, while line voltages, line currents, input power, shaft torque, speed and winding temperature are measured. After the load test, the motor is uncoupled from the dynamometer and a no-load test is performed, when the motor is fed at decreasing voltage levels, while line voltages, line currents, input power and winding temperature are recorded.

At each measured condition, the stator joule loss is calculated by (1), where m is the number of phases, I_1 is the line current and R_1 is the stator phase resistance corrected to the test temperature.

$$P_{j1} = mI_1^2 R_1 \quad (1)$$

From the no-load test data, the input power minus the stator joule loss is plotted against the squared line voltage, yielding a straight line whose intercept with the vertical axis equals the friction and windage loss. At each no-load test voltage level, the core loss is calculated as the input power minus the stator joule loss minus the friction and windage loss. An empirical relation between the core loss and the stator EMF is estimated considering the phase voltage approximately equal to the internal EMF at no-load.

At each load test point, the stator EMF is estimated through (2), where ϕ is the power factor angle, and employed with the empirical relation to determine the corresponding core loss.

$$E = \sqrt{(V_1 - R_1 I_1 \cos\phi)^2 + (R_1 I_1 \sin\phi)^2} \quad (2)$$

The airgap power P_{ag} at each load test point is calculated as (3), where P_{in} is the input power.

$$P_{ag} = P_{in} - P_{j1} - P_c \quad (3)$$

The rotor joule loss at each load test point is given by (4).

$$P_{j2} = sP_{ag} \quad (4)$$

The stray load loss (P_{sll}) at each load test point is roughly estimated through (5), where T is the measured shaft torque and ω_r is the shaft angular speed.

$$P_{sll} = P_{in} - T\omega_r - P_{j1} - P_c - P_{j2} - P_{fw} \quad (5)$$

Smoothed stray load loss values are obtained through (6), where A is the slope of the linear regression of the P_{sll} estimates against the squared torque. The regression is considered acceptable if the slope is positive and the determination coefficient (R^2) is greater than 0.9, even if it is necessary to exclude one data point.

$$P_{sll} = AT^2 \quad (6)$$

The total loss (P_L) at each load test condition is finally given by (7), and the efficiency (η) by (8).

$$P_L = P_{j1} + P_c + P_{j2} + P_{fw} + P_{sll} \quad (7)$$

$$\eta = \frac{(P_{in} - P_L)}{P_{in}} \quad (8)$$

IV. EXPERIMENTAL SETUP

Experimental data for the investigation were collected with the two-phase four-pole smooth solid rotor prototype depicted in Fig. 3, obtained by substituting the rotor of an available machine [28]. The rotor diameter was kept the same as the original reluctance rotor and its length matches the stator

stack length. There is no cooling fan attached to the rotor. The rated condition of the prototype was arbitrated as 138 V, 8 A at 200 Hz, and the constructive data of the machine are given in Appendix A.

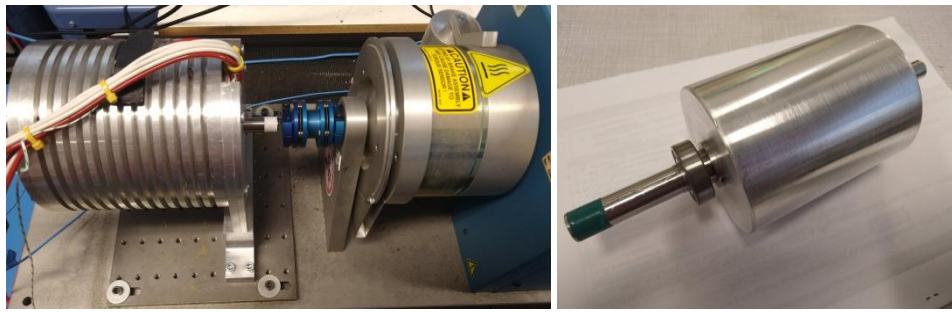


Fig. 3. SRIM prototype attached to the hysteresis brake (left) and smooth solid rotor (right).

Although SRIMs are usually supplied by solid state drives at high frequency, the time harmonics produce additional losses that complicate the experimental procedure. The machine was thus tested at grid frequency (50 Hz) with a reduced phase voltage of 34.6 V in order to keep the original V/f ratio and absolute slip speed to achieve the rated torque, as suggested in [2] and [29].

A scheme of the test setup is illustrated in Fig. 4. The SRIM is fed through a transformer array that converts the three-phase grid voltages into a balanced two-phase system, similarly as reported in [30]. A Magtrol hysteresis brake loads the motor and provides torque and speed measurements. Electrical measurements are performed by a HIOKI 3194 digital wattmeter. The stator coil resistance is measured in four-wire configuration with a digital DC supply and a voltmeter, and its temperature is monitored with a thermocouple. The estimated uncertainties of phase voltage, phase current, input power and torque at the tested conditions are circa 80 mV, 12 mA, 1 W and 5 mN.m, respectively.

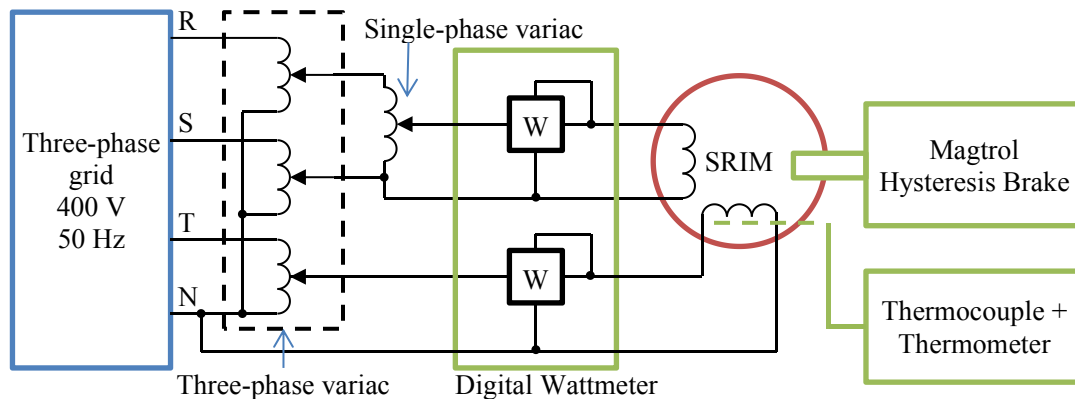


Fig. 4. Scheme of the experimental setup.

V. RESULTS

A. Stator resistance measurement

The cold (23.0°C) and hot average stator phase resistances were measured as 448 mΩ and 480 mΩ, respectively. The measurement was repeated before and after each test to determine the average value of R_1 to be used in stator joule loss calculations. All tests were performed as quickly as possible to limit temperature variations.

B. No-load test

A no-load test was performed at decreasing voltage levels starting from 125% of 34.6 V. The test was repeated with the motor coupled to the unpowered brake to check the speed variation. The resulting $P_{in} - P_{j1}$ curves of both no-load tests are illustrated in Fig. 5 along with the slip measured at the coupled no-load test.

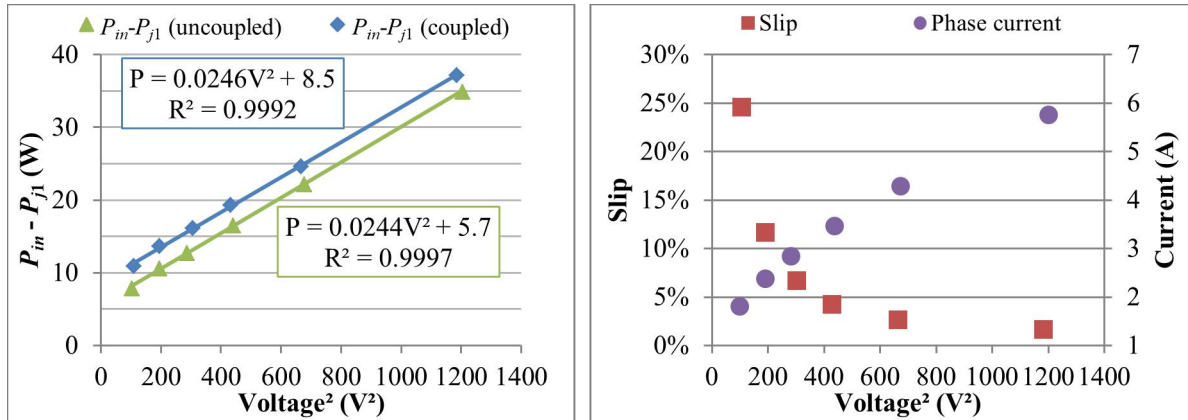


Fig. 5. Comparison of results from no-load tests (left) and slip and phase current measured at the coupled no-load test (right).

The comparison of the fitted curves in the left chart reveals initially a 2.8 W offset attributed to the dynamometer parasitic losses. The slip measured at the coupled no-load test, indicated in the right chart, reaches as high as 24 % without any visible increase in the line current. Even at rated voltage, a relatively high slip of 1.6% is observed. At slips this high, attributed to the high rotor resistivity, the rotor joule losses may not be neglected, and the friction and windage losses may not be considered constant.

The standard method was therefore adapted to account for these aspects as follows. The no-load input power $P_{in(NL)}$ is expressed in this case as (9).

$$P_{in(NL)} = P_{j1} + P_c + P_{j2} + P_{fw} \quad (9)$$

The friction loss is the load that causes the rotor to slip, thus it corresponds to the converted mechanical power being related to P_{j2} through (10).

$$P_{j2} = \frac{s}{1-s} P_{fw} \quad (10)$$

Since the tested motor has no fan, P_{fw} is caused mainly by friction, being fair to assume the linear dependence on the angular speed as expressed in (11), where P_{fw0} represents P_{fw} at synchronous speed.

$$P_{fw} = (1-s) P_{fw0} \quad (11)$$

Substituting (10) and (11) in (9), rearranging it and considering P_c proportional to V_1^2 by a constant k_c as in the standard, (12) is obtained. It shows that the intercept of the conventional line fit of $P_{in} - P_{j1}$ against V_1^2 equals not P_{fw} itself, but its hypothetical value at synchronous speed P_{fw0} .

$$P_{in} - P_{j1} = k_c V_1^2 + P_{fw0} \quad (12)$$

In the general case of a motor with a fan, if the windage loss is considered predominant, P_{fw} could be related to the slip through (13), and (14) would be finally obtained. Again, P_{fw0} could be determined from a line fit, although modified.

$$P_{fw} = (1 - s)^3 P_{fw0} \quad (13)$$

$$\frac{P_{in} - P_{j1}}{(1 - s)^2} = \frac{k_c V_1^2}{(1 - s)^2} + P_{fw0} \quad (14)$$

The core, friction and rotor joule losses determined through the adjusted procedure are indicated in Fig. 6. The linear expression relating the core loss and the squared phase voltage is used later during the load test. It must be noted that the stray no-load losses, i.e. losses caused by MMF and permeance harmonics at no-load condition, are accounted in P_c . The joule losses at slip frequency in the rotor core, usually included in P_c , are physically equivalent to P_{j2} in SRIMs.

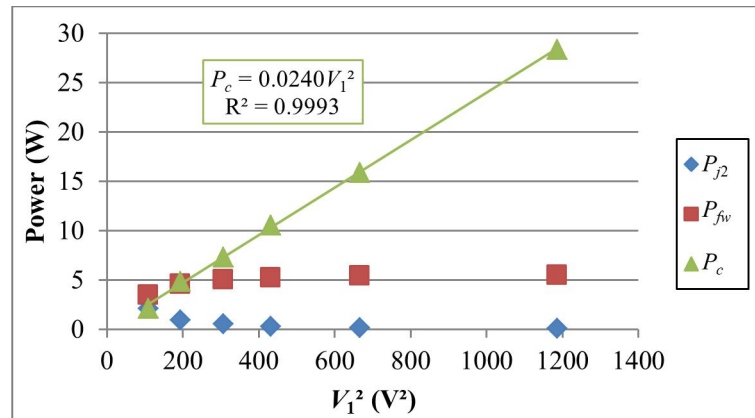


Fig. 6. Core, friction and rotor joule losses at different voltage levels in the no-load test.

C. Load test

The load test was performed at five points from 25 to 125% of the rated torque (0.8 N.m). The 150% level could not be reached due to limitations of the power supply.

A curious, yet not unexpected [17] result is illustrated in Fig. 7. Since the rotor power factor is practically constant, the current phasor locus in the complex plane forms a straight line, instead of an arc as in cage induction motors.

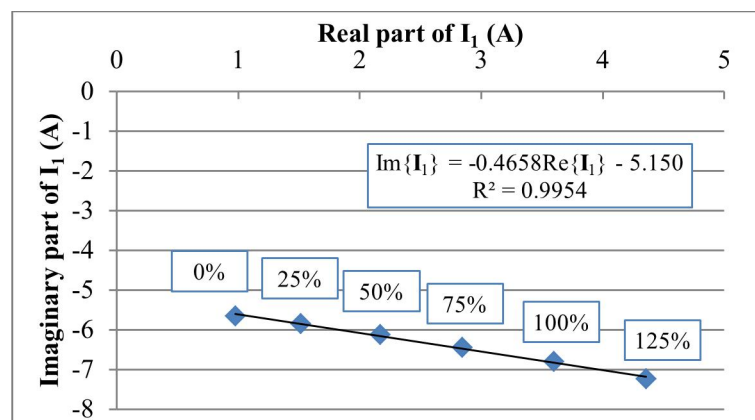


Fig. 7. Phase current locus in the complex plane at different levels of shaft torque.

For each point of the load test, P_{j1} was determined through (1), the stator EMF was calculated through (2) and applied to the linear relation indicated in Fig. 6 to determine P_c . Then, P_{j2} was calculated through (3) and (4), and P_{fv} through (10). The resulting values are indicated in the left chart of Fig. 8 according to the per-unit slip, that reached up to 40 % due to the reduced frequency. The

stray-load-loss determination is illustrated in the right chart and shows that, in order to satisfy the criterion of R^2 greater than 0.9, the last data point should be excluded.

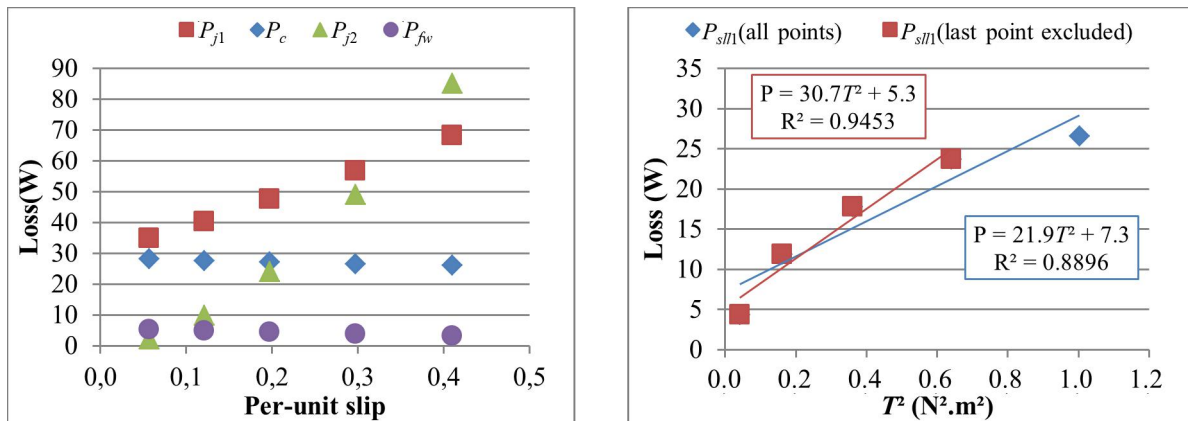


Fig. 8. Values of P_{j1} , P_c , P_{j2} and P_{fw} determined in the load test (left) and rough values of P_{stl1} plotted against the squared torque (right).

Yet, the plot does not deviate randomly from a straight line, but systematically as a second order polynomial, as if the stray-load losses did not increase linearly with the squared torque. Naturally, this behavior might be associated to measurement problems, but given the particularities of SRIMs, other hypotheses are drawn. As analyzed in [16] and in [9], stray losses depend mainly on the squared voltage and squared current, reflecting the flux and stator MMF. The portion present at no-load (stray-no-load loss) is accounted within P_c . When the load torque increases, so does the current, and the resulting increase in the stray losses corresponds to P_{stl} . Conventional cage or wound rotors present high power factor at low slip, thus I_ϕ and I_2 are practically in quadrature and (14) can be assumed. Assuming the excitation current practically constant and I_2^2 proportional to T^2 [11], (15) turns into a straight line equation relating I_1^2 to T^2 , justifying the standard process for loss segregation.

$$I_1^2 = I_\phi^2 + I_2^2 \tag{15}$$

In contrast, solid rotors present lower and almost constant power factor, therefore neither the quadrature between I_ϕ and I_2 nor (15) can be assumed. Moreover, as pointed out in the end of Section II, a larger variation of the stator EMF is expected in SRIMs, thus the excitation current may not be considered constant. Yet, the chart in Fig. 9 indicates that a linear relation between I_1^2 and T^2 is still present in the load test results, discarding this first hypothesis.

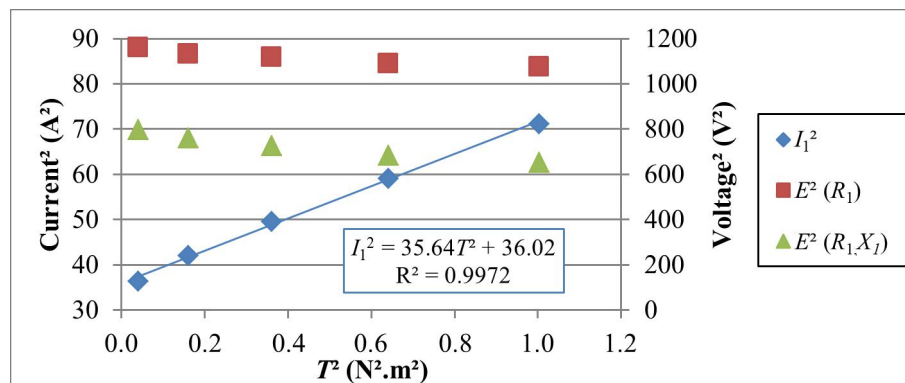


Fig. 9. Squared stator current and EMF (with and without the influence of X_1) plotted against squared torque in the load test.

A second hypothesis relates the stray loss behavior to a decrease in the stray-no-load loss as the current increases. The squared stator EMF calculated through (2) is also indicated by the square markers in Fig. 9 and shows a 7% reduction from the lowest to the highest torque level. These losses, however, are accounted within P_c , which is already corrected by E^2 . Still, (2) does not account for the voltage drop in the stator leakage reactance (X_1), which was estimated as 0.981 ohms at 50 Hz for this motor. The recalculation of the results considering the influence of X_1 yields new rough values of stray-load loss as presented in Fig. 10. The comparison with the original results does not show much difference, and this hypothesis was discarded.

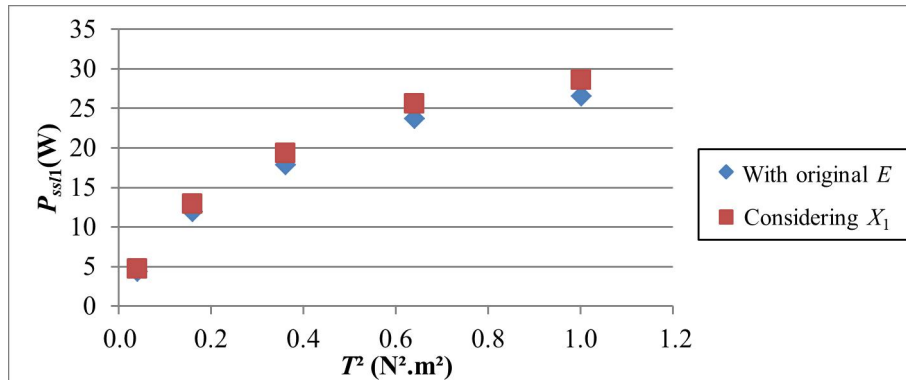


Fig. 10. Rough values of stray-load loss obtained according to the method of calculation of the stator EMF.

The third and current hypothesis is that the surface losses, which are part of the stray-load losses, are reduced as the slip increases. As indicated in the left chart of Fig. 8, the slip reached up to 40 % during the load test. As analyzed by [1], the airgap spatial harmonics that produce surface losses rotate at a lower speed than the fundamental rotating field. As the fundamental slip increases, the angular speed of these harmonics in the rotor tend to decrease, resulting in lower losses. This may explain why the increase in the stray-load losses decelerates as the torque increases, although further investigation is necessary for a definitive conclusion.

D. Loss and efficiency results

The slope identified in Fig. 8 was eventually employed to determine the stray-load losses of the tested motor. The complete segregation of losses as a function of the absolute slip speed is presented in the left chart of Fig. 11. The values of total loss and efficiency resulting from the loss segregation procedure are presented in the right chart and compared to the values measured directly, i.e. defining the output power as the product of the measured torque by the measured rotor speed. The closeness between the results of both methods indicates the success of the loss segregation procedure.

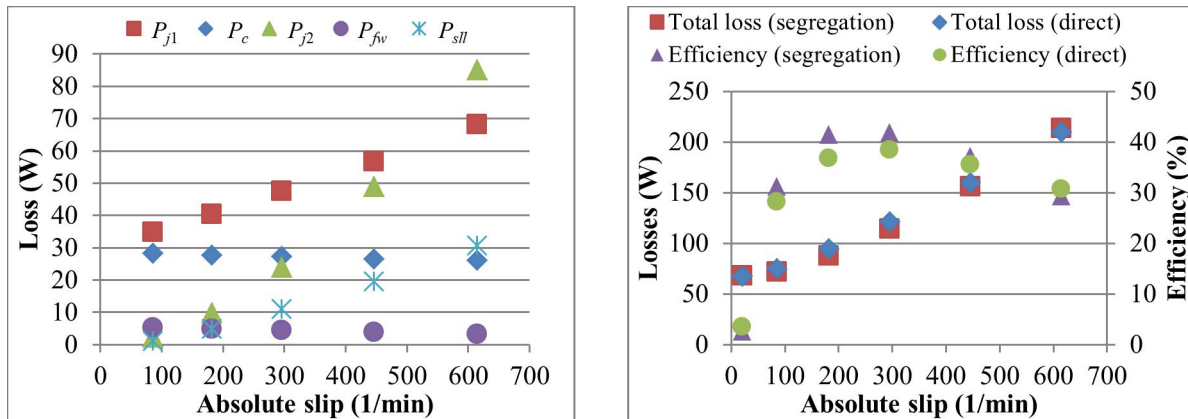


Fig. 11. Losses segregated at 50 Hz and resulting total losses and efficiency.

As indicated above, the tested motor achieved its maximum efficiency of 42 % at an absolute slip of 295 min^{-1} , with an output torque of 0.6 N.m. This apparently poor performance is due to the reduced frequency used in the test. If the motor was operated at its rated frequency and voltage, which are both four times those of the test, the airgap flux intensity would remain approximately the same, and the same torque of 0.6 N.m would be produced at an absolute slip of 295 min^{-1} . The rotational speed and consequently the output power would now be 4.73 times greater and, if the total loss remained the same, an efficiency of 75.8 % would be achieved at this absolute slip.

This raises a question: Do these results, obtained at reduced frequency, reflect the motor behavior at its rated condition? While some losses are expected to remain the same at a higher rotational speed with the same airgap flux intensity, some do not. In the same way as the torque, the rotor joule losses depend on the airgap flux intensity and on the absolute slip speed, remaining the same as in the test. As the airgap flux and the torque are the same, so do the magnetization and load currents and, consequently, the phase current and the stator joule losses. Even though the same induction levels are expected in the stator core, higher core losses will be produced due to the higher frequency. The increased rotational speed will also produce higher friction and windage losses. The angular speed of the MMF and permeance space harmonics increases proportionally to the supply frequency [1], therefore the respective surface losses might remain approximately the same, although the complexity of the stray loss mechanisms hinders any prediction. Since solid state drives are usually employed in this case, the core losses are also expected to increase due to the involved time harmonics.

Even though it might seem that the validity of the loss segregation is compromised, the application of its results to the rated condition is simple. As analyzed by [9], the no-load component tends to dominate the stray losses. Therefore, all loss components that are expected to increase (core, friction, windage and stray no-load loss) are practically constant with respect to the slip and may thus be corrected through a simple no-load test at rated condition. Unfortunately, this procedure could not be carried out due to infrastructure limitations, but may be pursued in future works.

VI. CONCLUSION

In this paper, the applicability of standard methods for loss segregation in induction motors has been analyzed in the context of motors with solid rotors. A two-phase smooth solid rotor induction motor prototype was subjected to the tests described in the IEEE Standard 112 method B and the results were analyzed in the light of the theoretical aspects presented in Section II.

Although these motors are designed for high frequency supplies, the loss segregation procedure was performed at a reduced frequency in order to avoid the effects of time harmonics originated from solid state drives. The airgap flux intensity was kept close to the rated condition by adjusting the voltage accordingly.

The first irregularity to be detected was the excessive slip during the no-load test, which disqualifies the assumptions of negligible rotor joule losses and constant friction and windage losses. It was shown that, in the case of a fanless motor, the typical separation of no-load losses yields the hypothetical value of P_{fw} at synchronous speed.

The results of the load test indicated that the standard procedure for the determination of stray-load losses may be inadequate in reduced frequency tests, since the large variation of the per-unit slip affects the behavior of the surface losses. Computational investigations of the surface loss behavior as a function of slip may contribute to the resolution of this question.

The validity of the reduced frequency test results was analyzed for the rated condition. Even though it was not possible to demonstrate it experimentally, it was suggested that the test results can be corrected for the rated condition through a simple no-load test with a high-frequency power supply. This may be demonstrated in future works, when the laboratorial limitations are overcome.

APPENDIX

The constructive data of the tested motor is indicated in Table I.

TABLE I. CONSTRUCTIVE DATA OF THE TESTED MOTOR.

Description	Value
Number of phases	2
Number of poles	4
Rotor diameter (mm)	79
Rotor length (mm)	100
Rotor material	XC18
Rotor conductivity (S/m)	6.25E+6
Air-gap length (mm)	0.5
Stator active length (mm)	100
Stator outer diameter (mm)	123
Stator slot number	16
Conductors per slot	30
Winding type	Concentrated

ACKNOWLEDGMENT

The authors would like to thank Coordenação de Aperfeiçoamento de Pessoal de Nível Superior – Brazil (CAPES/COFECUB Ph 930-19 Fin. code 88881.191763/2018-01) and CNPq – the Brazilian Research Council for partially funding this study.

REFERENCES

- [1] J. Hupponen, “High-speed solid-rotor induction machine – electromagnetic calculation and design,” *Ph.D. dissertation*, Lappeenranta University of Technology, Lappeenranta, Finland, 2004.
- [2] J. Pyrhonen, J. Nerg, P. Kurronen and U. Lauber, “High-Speed High-Output Solid-Rotor Induction-Motor Technology for Gas Compression,” *IEEE Trans. on Ind. Electronics*, vol. 57, no. 1, pp. 272-280, Jan. 2010.
- [3] J. F. Gieras and J. Saari, “Performance Calculation for a High-Speed Solid-Rotor Induction Motor,” *IEEE Trans. on Industrial Electronics*, vol. 59, no. 6, pp. 2689-2700, June 2012.
- [4] L. A. Finzi and D. A. Paice, “Analysis of the Solid Iron Rotor Induction Motor for Solid-State Speed Controls,” *IEEE Trans. on Power Apparatus and Systems*, vol. PAS-87, no. 2, pp. 590-596, Feb. 1968.
- [5] L. Papini, C. Gerada, D. Gerada and A. Mebarki, “High speed solid rotor induction machine: Analysis and performances,” in *17th Int. Conf. on El. Machines and Sys. (ICEMS)*, Hangzhou, China, 2014, pp. 2759-2765.
- [6] J. R. Bumby, E. Spooner and M. Jagiela, “Equivalent circuit analysis of solid-rotor induction machines with reference to turbocharger accelerator applications,” *IEEE Proc. - Electric Power Applications*, vol. 153, no. 1, pp. 31-39, Jan. 2006.
- [7] B. J. Chalmers and I. Woolley, “General theory of solid-rotor induction machines,” *Proc. of the Institution of Electrical Engineers*, vol. 119, no. 9, pp. 1301-1308, September 1972.
- [8] C. Mellak, J. Deuringer and A. Muetze, “Impact of Aspect Ratios of Solid Rotor, Large Air Gap Induction Motors on Run-Up Time and Energy Input,” in *IEEE Trans. on Industry Applications*, 2022, doi: 10.1109/TIA.2022.3180030.
- [9] E. Spooner, “Stray loss in solid-rotor induction machines,” *IEE Proc. B - Electric Power Applications*, vol. 129, no. 4, pp. 181-189, July 1982.
- [10] M. Jagiela, J. Bumby, and E. Spooner, “Time-domain and frequency-domain finite element models of a solid-rotor induction/hysteresis motor,” *IET electric power applications*, vol. 4, no. 3, pp.185-197, 2010.
- [11] Standard Test Procedure for Polyphase Induction Motors and Generators, *IEEE Standard 112*, 2018.
- [12] International Standard IEC 60034-2-1, “Rotating electrical machines - Part 2-1: Standard methods for determining losses and efficiency from tests (excluding machines for traction vehicles),” 2014.
- [13] M. Fratila, A. Benabou, A. Tounzi and M. Dessoude, “Calculation of Iron Losses in Solid Rotor Induction Machine Using FEM,” in *IEEE Transactions on Magnetics*, vol. 50, no. 2, pp. 825-828, Feb. 2014.
- [14] M. S. Sarma and G. R. Soni, “Solid-Rotor and Composite-Rotor Induction Machines,” *IEEE Trans. on Aerospace and Electronic Systems*, vol. AES-8, no. 2, pp. 147-155, March 1972.
- [15] N. D. Sharma, R. Anbarasu, J. Nataraj, A. Y. Dangore and B. Bhattacharjee, “Experimental investigations on high speed solid and composite rotor induction motor,” in *Proc. of Int. Conf. on Power Electronics, Drives and Energy Systems for Industrial Growth*, New Delhi, India, vol.2, pp. 913-919, 1996
- [16] K. K. Schwarz, “Survey of basic stray losses in squirrel-cage induction motors,” *Proc. of the Inst. of Electrical Engineers*, vol. 111, no. 9, 1964.
- [17] W. J. Gibbs, “Induction and synchronous motors with unlaminated rotors,” *Journal of the Institution of Electrical Engineers - Part II: Power Engineering*, vol. 95, no. 46, pp. 411-420, August 1948.
- [18] H. M. McConnell, “The Polyphase Induction Machine with Solid Rotor,” *Trans. of the American Inst. of Electrical Engineers. Part III: Power Apparatus and Systems*, vol. 72, no. 2, pp. 103-111, April 1953.
- [19] H. M. McConnell and E. F. Sverdrup, “The Induction Machine With Solid Iron Rotor,” *Trans. of the American Ins. of Electrical Engineers, Part III: Power Apparatus and Systems*, vol. 74, no. 3, pp.343-349, 1955.
- [20] P. D. Agarwal, “Eddy-current losses in solid and laminated iron,” *Trans. of the American Inst. of Electrical Engineers, Part I: Communication and Electronics*, vol. 78, no. 2, pp. 169-181, 1959.
- [21] K. P. P. Pillai, “Fundamental-frequency eddy-current loss due to rotating magnetic field. Part 1: Eddy-current loss in solid rotors,” *Proc. of the Inst. of Electrical Engineers*, vol. 116, no. 3, pp. 407-410, March 1969.
- [22] G. Angst, “Polyphase Induction Motor with Solid Rotor; Effects of Saturation and Finite Length,” *Trans. of the American Institute of Electrical Engineers. Part III: Power Apparatus and Systems*, vol. 80, no. 3, pp. 902-909, April 1961.
- [23] H. Yee and T. Wilson, “Saturation and finite-length effects in solid-rotor induction machines,” *Proc. of the Institution of Electrical Engineers*, vol. 119, no. 7, pp. 877-882, July 1972.
- [24] K. Boughrara, F. Dubas and R. Ibtouen, “2-D Analytical Prediction of Eddy Currents, Circuit Model Parameters, and Steady-State Performances in Solid Rotor Induction Motors,” *IEEE Trans. on Magnetics*, vol. 50, no. 12, pp. 1-14, Dec. 2014.
- [25] N. Kesavamurthy and P. K. Rajagopalan, “Equivalent Circuit and Evaluation of Eddy-Current Loss in Solid Cores subjected to Alternating and Rotating Magnetic Fields,” in *Proc. of the IEE - Part C: Monographs*, vol. 107, no. 12, pp. 353-361, September 1960.
- [26] R. Yang, L. Zhou, J. Wang, Y. Xiao and Z. Ling, “Performance calculation for a canned solid-rotor induction motor with squirrel-cage,” in *20th Int. Conf. on Electrical Machines and Systems (ICEMS)*, Sydney, Australia, pp. 1-5, 2017.

- [27] C. Di, I. Petrov and J. J. Pyrhönen, “Modeling and Mitigation of Rotor Eddy-Current Losses in High-Speed Solid-Rotor Induction Machines by a Virtual Permanent Magnet Harmonic Machine,” in *IEEE Transactions on Magnetics*, vol. 54, no. 12, pp. 1-12, Dec. 2018.
- [28] S. Yammine, C. Henaux, M. Fadel, and F. Messine, “Torque Ripple Reduction in a SynRM at a Constant Average Torque by Means of Current Harmonics Injection,” *Progress In Electromagnetics Research C*, vol. 80, 167-180, 2018.
- [29] T. Aho, J. Nerg and J. Pyrhonen, “Experimental and Finite Element Analysis of Solid Rotor End Effects,” *IEEE International Symposium on Industrial Electronics*, Vigo, Spain, pp. 1242-1247, 2007.
- [30] C. van der Merwe and F. S. van der Merwe, “A study of methods to measure the parameters of single-phase induction motors,” *IEEE Trans. on Energy Conversion*, vol. 10, no. 2, pp. 248-253, June 1995.